


FULL PAPER

Open Access



Mid-infrared imaging spectroscopic measurements of C₂H₄ frost simulating the outer solar system environments

Ryoichi Koga^{1*} , Shohei Negishi¹, Biao Zhao¹, Yuan Li¹, Fumiyuki Ito², Yasumasa Kasaba³ and Yasuhiro Hirahara¹

Abstract

In the dense and cold atmosphere of Titan, the presence of C₂H₄ haze has been confirmed by the observations of spacecraft. In the present study, original cryogenic experimental equipment was developed to simulate the low-temperature solid formation of C₂H₄ in combination with in-situ infrared spectroscopic measurements. As a result, out-of-plane bending vibration ν_7 of solid-phase C₂H₄ located at $\sim 10.5 \mu\text{m}$ was successfully detected with high sensitivity, and two-dimensional spectrographs of C₂H₄ at low temperatures were obtained. The obtained spectra of C₂H₄ can be fitted to the double Lorentzian function with various heights, central wavelengths, and full widths at half the maximum (FWHM) of the two-component Lorentzian functions. They were classified into three types using the fitting parameters. However, their spectral shapes are different from the amorphous, metastable, and crystalline forms obtained by the previous laboratory experiment in terms of the distance of two peak wavelengths and FWHM. The results may link to understanding the spectral band properties of C₂H₄ condensation in the haze component of Titan.

*Correspondence:

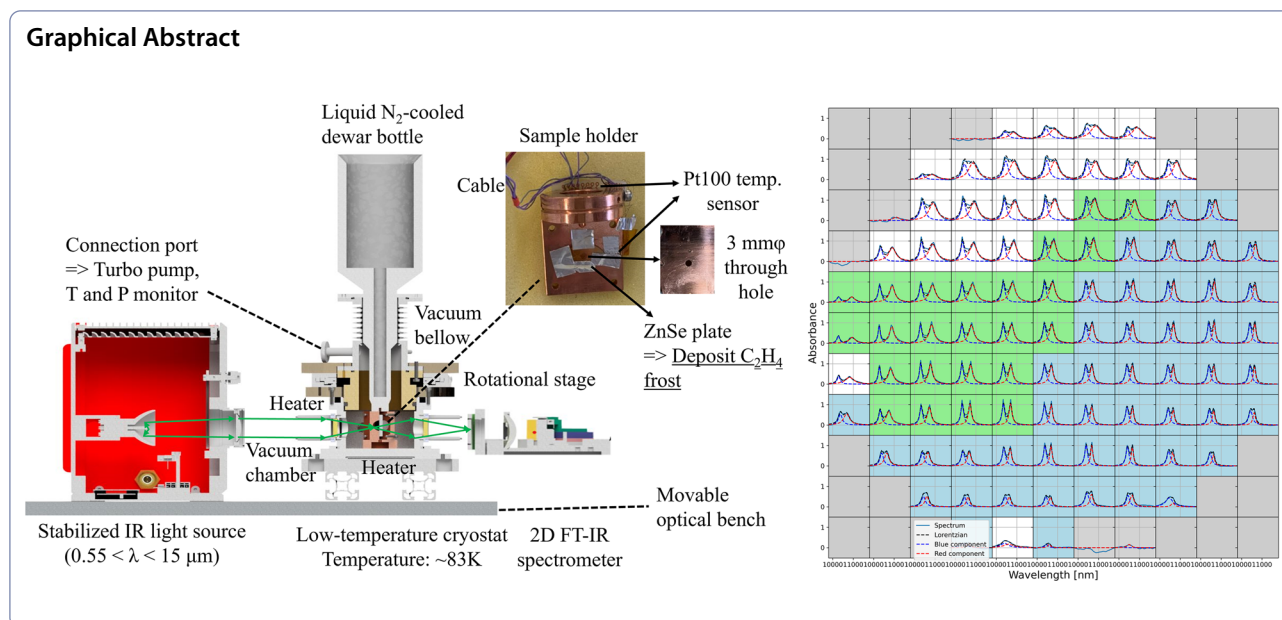
Ryoichi Koga

koga.ryoichi.y9@a.mail.nagoya-u.ac.jp

Full list of author information is available at the end of the article



© The Author(s) 2024. **Open Access** This article is licensed under a Creative Commons Attribution 4.0 International License, which permits use, sharing, adaptation, distribution and reproduction in any medium or format, as long as you give appropriate credit to the original author(s) and the source, provide a link to the Creative Commons licence, and indicate if changes were made. The images or other third party material in this article are included in the article's Creative Commons licence, unless indicated otherwise in a credit line to the material. If material is not included in the article's Creative Commons licence and your intended use is not permitted by statutory regulation or exceeds the permitted use, you will need to obtain permission directly from the copyright holder. To view a copy of this licence, visit <http://creativecommons.org/licenses/by/4.0/>.



Introduction

The atmosphere of Saturn's largest moon Titan is a dense layer of gases with ~ 1.5 atm at the surface, which is the thickest among all satellites. Titan's lower atmosphere is primarily composed of nitrogen (94.2%) and the simplest hydrocarbon, methane (5.65%). Since the temperature of the atmosphere is as low as ~ 90 K (Mitri et al. 2007), Titan's atmosphere supports opaque haze layers blocking most visible light from the Sun. The first observation of Titan's atmosphere was conducted by the Voyager I spacecraft (Smith et al. 1982). Titan's atmosphere has a complex system of atmospheric variability, especially the asymmetric north–south haze has been intensively investigated (Lorenz et al. 1999). Further information about the composition and character of Titan's atmosphere is summarized in Hörst (2017).

According to the phase diagram of ethylene (C_2H_4) calculated by Fray & Schmitt (2009) using thermodynamic equations in their study of sublimation and condensation of ice in planetary systems, it can be seen that ethylene is solid at the temperature and atmospheric pressure conditions of Titan. Roe et al. (2004) reported the spatially resolved chemical abundance of hydrocarbon in Titan's atmosphere observed by the W.M. Keck I 10-m telescope. They showed the seasonal change and significant accumulation of C_2H_4 gas in the south polar stratosphere. Recently, the content of C_2H_4 was found to be 3.91 ppm in Titan's atmosphere located at 1050 km from the surface, using Cassini's mass spectrometer (Magee et al. 2009). In other celestial bodies, C_2H_4 was detected during the New Horizon flyby at Pluto (Gladstone et al. 2016).

Haze particles dominated by C_2 hydrocarbon C_2H_2 , C_2H_4 , and C_2H_6 settle out on Pluto's surface (Grundy et al. 2018). C_2H_4 was also detected in the interstellar environment of CRL 618 (Cernicharo et al. 2001). There is a feasibility study that aims for future spacecraft missions such as Europa Clipper to detect the hydrocarbon in the Jupiter system (Teolis et al. 2017).

Previous laboratory experiments showed the condition to form the various solid phases of C_2H_6 (Hudson et al. 2009). However, the processes of morphological changes in solid C_2H_4 are less clear than in C_2H_6 . Jacox (1962) first observed the laboratory infrared vibration absorption spectra of solid-phase C_2H_4 in low temperatures. They found significant differences in the position, splitting, and linewidth of the absorption peaks at 4 K and 53 K. Rytter & Gruen (1979) conducted the matrix isolation experiment at 15 K and annealing at 85 K to interpret the data in terms of a monomer, dimer, aggregate, and crystal scheme. They characterized a transformation between two crystalline phases. The 823 and 1434 cm^{-1} bands are assigned to a low-temperature form and 820, 826, and 1436 cm^{-1} to a high-temperature form. Nes & Vos (1979) determined the single-crystal structure of C_2H_4 at 85 K by X-ray diffraction method. They suggested that there are two non-equivalent C_2H_4 molecules in the unit lattice. Molecules on the sides of the cube are oriented in the same direction, only the molecular in the center is not parallel to the other molecules. Later, Hudson et al. (2014) measured the bending vibration ν_7 , ν_{10} , and ν_{12} of solid C_2H_4 with a thickness of 1 μm . They concluded that the various vibration spectra are attributable

to three solid forms. The crystalline C_2H_4 ice was created by a slow deposit ($1 \mu m h^{-1}$) at 60 K and then cooled to 20 K. The metastable ice was created by a fast deposit ($60 \mu m h^{-1}$) at 20 K. The amorphous ice was created by a slow deposit ($1 \mu m h^{-1}$) at 12 K and then heated to 20 K. They also conducted the annealing experiment of the amorphous C_2H_4 sample from 12 to 60 K. The spectral shapes changed near 35 K and again near 50 K, which showed the amorphous phase changed to a high-temperature crystalline phase. Especially, the small 822-cm^{-1} band was found to be a very sensitive indicator of phase changes. Molpeceres et al. (2017) also measured the physical and spectroscopic properties of ices of mixed C_2H_4 and CH_4 , which possibly simulated Pluto's surface.

Spectra in the previous experiments were averaged over an aperture range of a few mm or more, and it was not possible to determine whether the spectra varied by location on the deposited plate surface. In this study, we measured the spatially resolved mid-infrared spectra of solid C_2H_4 in sub-millimeter for the first time. According to the model spectrum shown in Fig. 5 of Roe et al. (2004), there are CH_4 , C_2H_4 , C_2H_6 , and C_2H_2 , whose peak wavelengths are about 7.6, 10.5, 12.1, and 13.5 μm , respectively. However, in this paper, we selected C_2H_4 , which is the most suitable target for measurement, because the wavelength range of the imaging spectrometer guaranteed by the manufacturer is $8 \mu m < \lambda < 12 \mu m$.

Experimental procedures

An original cryogenic optical equipment was developed for conducting laboratory simulation of low-temperature C_2H_4 solid formation with *in-situ* infrared spectroscopic measurement, as shown in Fig. 1. The vacuum chamber was fabricated using a 5-axis simultaneous machining center at the Nagoya University Instrument Development Center. The heaters were equipped at the bottom and top of the chamber. The liquid N_2 cooling dewar bottle was mounted on the upper part and directly connected to the oxygen-free high-conductivity copper (OFHC) sample holder with a center through hole of ~ 3 mm in diameter. The sample holder adopted with the cold head was cooled to ~ 90 K. A 1 mm-thick ZnSe crystal plate was attached to the OFHC sample holder and covered the center hole for the infrared transmissive substrate. The stabilized silicon nitride globar lamp unit (SLS303, Thorlabs Co.) was used for the high emittance light source in the wavelength range $0.55 < \lambda < 15 \mu m$. In the middle of the cryostat, there was the vacuum bellow with six ports. One of them is connected to the equipment including the turbo pump, pressure monitor, and valve. Another port was covered by a hermetic seal with four terminals. It connected the Pt100 sensor near the ZnSe plate and the electric circuit outside the chamber using the cable. The resistance of Pt100 was read by the 4-terminal method, and then, the temperature corresponding to the resistance was calculated.

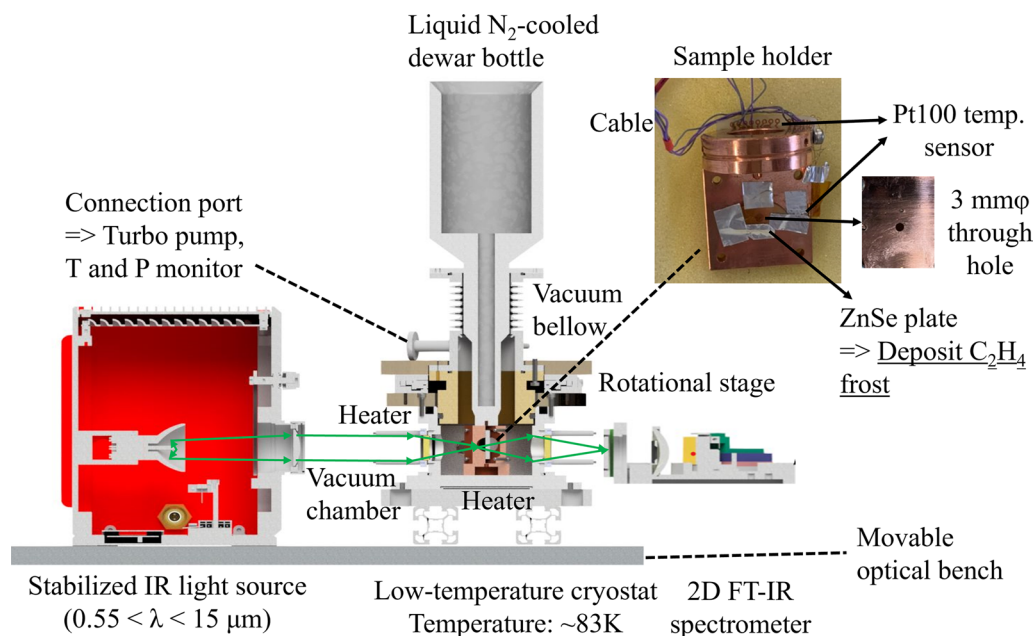


Fig. 1 Schematic diagram of experimental setting seen from the side

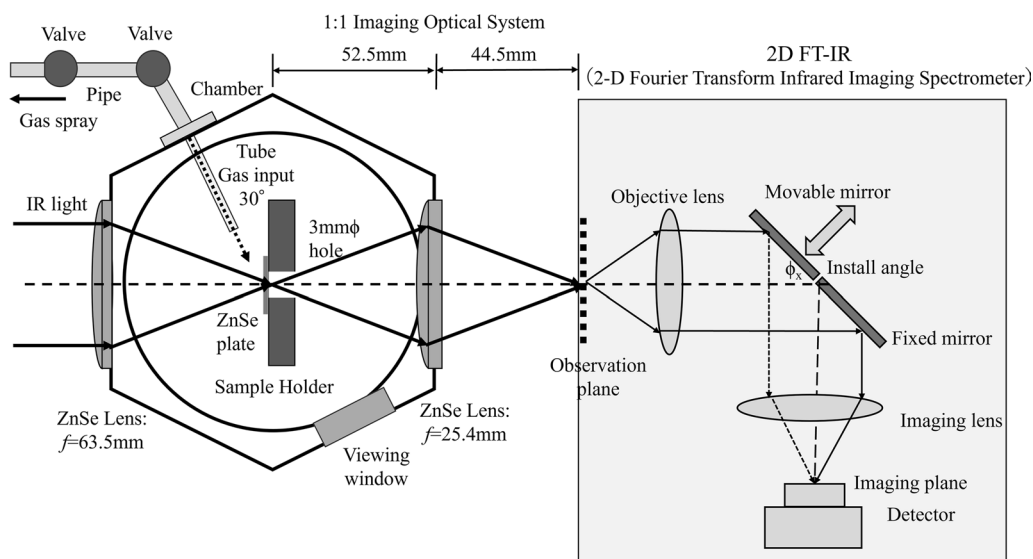


Fig. 2 Top view of a near-equivalent imaging optical system constructed by IR light source, vacuum chamber, and 2D FT-IR

As shown in Fig. 2, we constructed the near-equivalent optical system between the sample plate and detector by employing appropriate two ZnSe lens windows. The distance from the chamber to the spectrometer can be optimized by the movable optical bench. Transmittance spectral measurements were conducted by employing the imaging Fourier transform mid-infrared spectrometer (2D FT-IR, NISSIN KIKAI NK-0812-TD-NU). The operation principle of 2D FT-IR is a common-optical path wavefront splitting-type phase shift interferometry. It enables the easy acquisition of infrared spectral images instantaneously by adopting the focal plane array detector (Inoue et al. 2006). The interference-pattern visibility is optimized by a suitable design of the multi-slit array, which is based on the theories of Fraunhofer diffraction and convolution imaging (Qi et al. 2015). The input light is collimated and incident as a parallel beam to the Fourier transform plane and then reflected at a certain installation angle of the movable and fixed mirrors to the focal plane array detector through the

objective lens. The detector mounted in the imaging spectrometer is the bolometer camera (Boson, FLIR Co.) operating in the ambient temperature condition, in which the number of pixels is 640×512 with a pixel size of $12 \mu\text{m}$. The wavelength resolution of 2D FT-IR is $\sim 70.7 \text{ nm}$, which corresponds to 7 cm^{-1} at $10 \mu\text{m}$. The 800 frames IR image data set in the time domain are obtained subsequently during the linear motion of the phase shifter and then are Fourier-transformed to acquire the frequency domain data by applying the fast Fourier transform (FFT) method for each pixel data to obtain a two-dimensional spectral image.

Table 1 summarizes the conditions of measurement and Fig. 3 shows the procedure of the experiment. Before the experiment, the inside of the chamber was heated for 1 h to evaporate the remnant water and eject it. The rotational stage and vacuum below were adjusted so that the image of a $3\text{mm}\phi$ hole appeared in the field of view. For the production of low-temperature solid C_2H_4 before the spectroscopic measurement, the vacuum chamber

Table 1 Summary of the experimental properties

Elapsed time from first gas input	Elapsed time from second gas input	Target	Chamber pressure (Pa)	C_2H_4 input pressure (Pa)
–	–	BPF	–	–
–	–	ZnSe plate	0.24	–
1 min	–	ZnSe + C_2H_4	1200	700
10 min	–	ZnSe + C_2H_4	1600	700
26 min	1 min	ZnSe + C_2H_4	3000	1000
35 min	10 min	ZnSe + C_2H_4	3670	1000

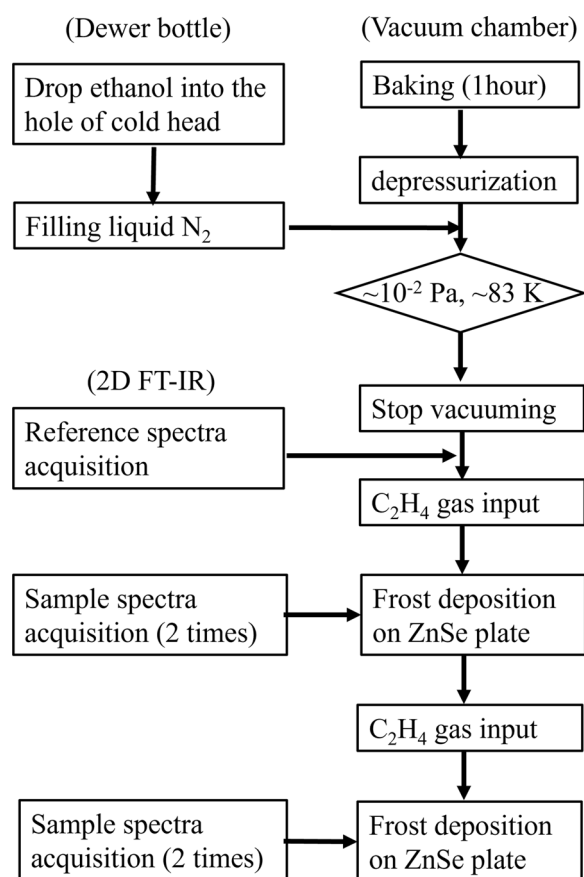


Fig. 3 Flow chart of the experimental procedure

was initially pumped out to reach $\sim 10^{-2}$ Pa using the turbo-molecular pump (TSU-261, Pfeiffer Co.). A small amount of ethanol was dropped into the hole of the cold head. Then the liquid N_2 coolant was poured into the dewar bottle. Approximately 10 min after filling the coolant, the ZnSe substrate temperature was lowered to ~ 83 K. The temperature change was within 10 K through the experiment. The valve which connected to the pump was closed and the vacuuming was stopped at this time. Then, the blank measurement was conducted to acquire the reference spectra. Unfortunately, the natural leak occurred with a leak rate of ~ 40 Pa/min. However, the influence of absorption of the atmosphere was not large, because the wavelength of major absorption of atmospheric CO_2 is 14–15 μm , which is different from that of C_2H_4 . Twenty-five minutes later, the pure C_2H_4 gas sample enclosed in the spray can (GL Science Co., 99.5% purity) was introduced into the pipe between two valves. Then, it was introduced into the chamber at a 30° angle from the ZnSe plate through the tube whose inner diameter is 1.5 mm. The displayed value of the pressure gauge increased from 500 to 1200 Pa at this moment. C_2H_4 input pressure inside the chamber is defined as

this difference of 700 Pa. Immediately after the input to the chamber, gas touched the cold plate and then it condensed. 26 min after the first gas input, the gas was introduced into the chamber repeatedly. The displayed value of the pressure gauge at the second gas input increased from 2700 to 3000 Pa. Therefore, the total C_2H_4 input pressure is calculated as $700 + 300 = 1000$ Pa. 2D FT-IR measurements to acquire the sample spectra were conducted 1 and 10 min after the first gas input, and 1 and 10 min after the second gas input (26 and 35 min after the first gas input). Because the deposition rate of C_2H_4 was unknown before measurement, the pump out of the chamber before the measurements was not conducted in this experiment.

NISSIN KIKAI Co. provided the software Spectro-Viewer which was used to obtain the spectrum from the interferogram at each pixel. It is useful to acquire a quick look at the measurement results but is inconvenient to execute advanced spectral analysis such as baseline correction, creating a spectral map, and fitting. Therefore, we referred to several papers about the application of 2D FT-IR (Nogo et al. 2016, 2021; Qi et al. 2015; Qi 2016) and the Japanese patent (Ishimaru 2012), and developed the data analysis program to convert raw interferogram data to a 3D spectral data cube. The summary of the algorithm is shown in Fig. 4. The interferogram of each pixel was shifted so that the maximum value is at the center of the array, which is called a center-burst correction [e.g., Polavarapu (1985)]. Then, interferogram $f(n)$ is multiplied by Hamming window function $w(n)$:

$$x(n) = f(n)w(n) \quad (1)$$

$$w(n) = 0.54 - 0.46 \cos\left(\frac{2\pi n}{N-1}\right) \quad (2)$$

where N is number of pictures. The number of elements increased from $N=800$ to $N'=4096$ by adding 0 at both ends of the interferogram. This operation, called zero-filling, is shown in Fig. 5. Finally, the interferogram is converted into the array $y(k)$ by fast Fourier transform (FFT):

$$y(k) = \sum_{n=0}^{N-1} e^{-2\pi i \frac{kn}{N'}} x(n) \quad (3)$$

The absolute value of the array $y(k)$ is the relative intensity spectrum. Zero-filling can increase the data points of the spectra before linear interpolation. Although the spectral resolution does not improve, it is useful to compare the spectral shapes with each other.

Wavelength calibration was done in this experiment to determine the install angle of the movable and fixed

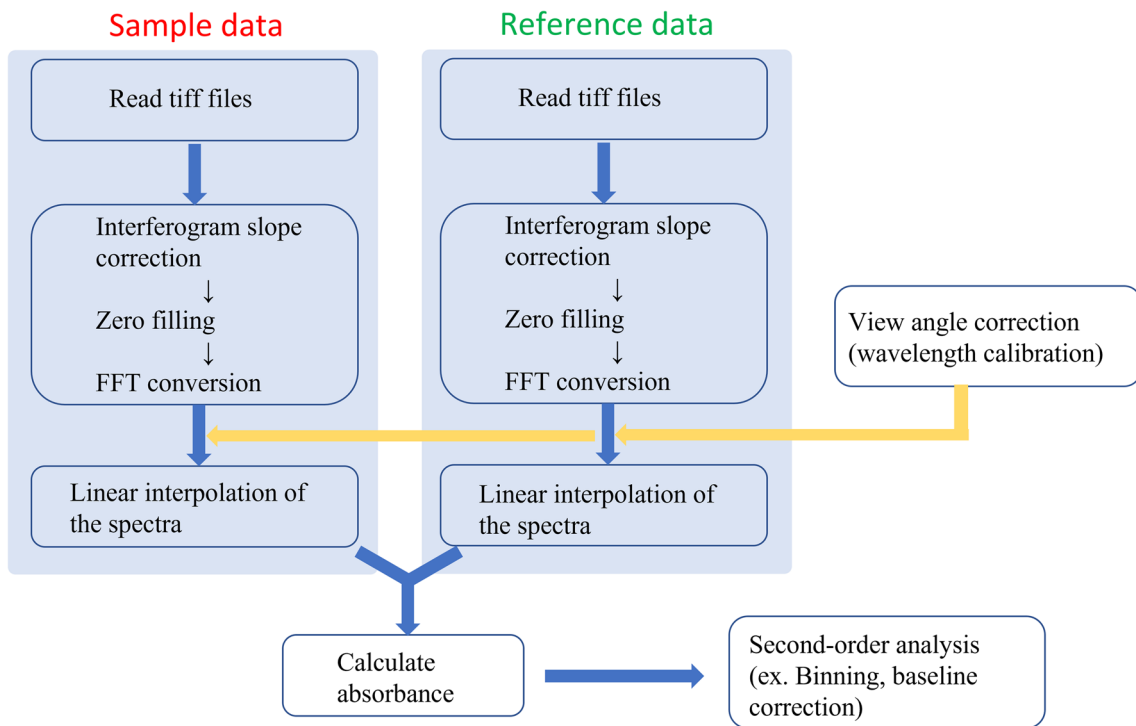


Fig. 4 Flow chart of the data analysis algorithm

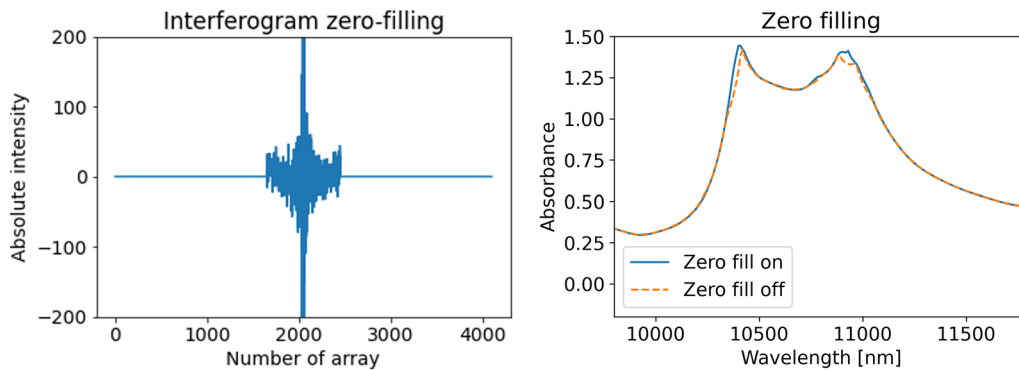


Fig. 5 (Left) Zero-filling of the interferogram. (Right) Spectra acquired by FFT of the interferogram with and without zero filling

mirrors ϕ_x using the technique of view angle correction, which is shown in Qi (2016). The optical path length difference L of the light received by the pixel at the center position of the detector can be represented as

$$L = 2M \cos(\phi_x - 90^\circ) \tag{4}$$

where M is the moving distance of the mirror. When calculating the phase difference for any given pixel except for the center position of the detector, it is necessary to calculate the view angle of the light incident on the phase shifter. In case the pixel at the center of the detector is

taken as the origin, the x and y components at any pixel (a, b) can be represented as

$$a = (n_x - 320)s_{\text{pix}} \tag{5}$$

$$b = -(n_y - 256)s_{\text{pix}} \tag{6}$$

where n_x , and n_y are pixel numbers on x and y coordinates, which are defined as the horizontal and vertical direction on the imaging plane, respectively [see also Fig. 1 of Qi et al. (2015)]. At the origin of the pixel, $n_x = 320$ and $n_y = 256$. s_{pix} is the pixel size of the detector

of 12 μm. View angle on x and y coordinates can be represented as

$$\theta_x = \tan^{-1}(a/f) \tag{7}$$

$$\theta_y = \tan^{-1}(b/f) \tag{8}$$

where $f=25$ mm is focal distance of the imaging lens. The optical path length difference after view angle correction L' can be represented as

$$L' = \{2M \cos(\phi_x - \theta'_x)\} / \cos \theta_y \tag{9}$$

$$\theta'_x = \theta_x + 90^\circ \tag{10}$$

For wavelength calibration, light from the same source was transmitted in a narrow bandpass filter (BPF) Spectrogon NB-9585–135 and a blank spectrum was measured by 2D FT-IR. The known transmittance data of this BPF is plotted as blue dots in the upper left panel of Fig. 6. When the installation angle was $\phi_x=44.874^\circ \pm 0.016^\circ$, the relative intensity spectrum at the center pixel $(n_x, n_y)=(320, 256)$ shown as the red solid line could be best fitted to the BPF transmittance data. The right panel of Fig. 6 shows the spectrum map with 7×7 bins of the light passing through BPF

in the case of $\phi_x=44.874^\circ$. The spectrum of one bin is averaged in the range of 35×35 pixels. In bins where the signals were detected, the peaks of the spectrum are in the range of 9590–9620 nm. The difference between the peaks is smaller than the wavelength resolution of 2D FT-IR. Therefore, the wavelength calibration is thought to be adequate.

Relative intensities at 0.01 μm intervals in the 7–14 μm range are calculated by linear interpolation based on the wavelength array determined by view angle correction. The absorbance spectrum at each pixel can be represented as

$$Z(n_x, n_y, z) = \log_{10} \left(\frac{Z_{\text{ref}}(n_x, n_y, z)}{Z_{\text{sam}}(n_x, n_y, z)} \right) \tag{11}$$

Z_{ref} and Z_{sam} are the relative intensity data cubes of reference and sample, z is the number of images that corresponds to the optical path length difference. Image data cube of Z_{ref} and Z_{sam} obtained by 2D FT-IR are explained in Fig. 2 of Nogo et al. (2021). The baseline undulation was corrected to eliminate the influence such as absorption of natural leaks and outgas from the frost. As shown in Fig. 7, linear interpolations with zero-order (linear), first-order, and second-order polynomials were performed using the spectrum in the range of 7.0–9.8

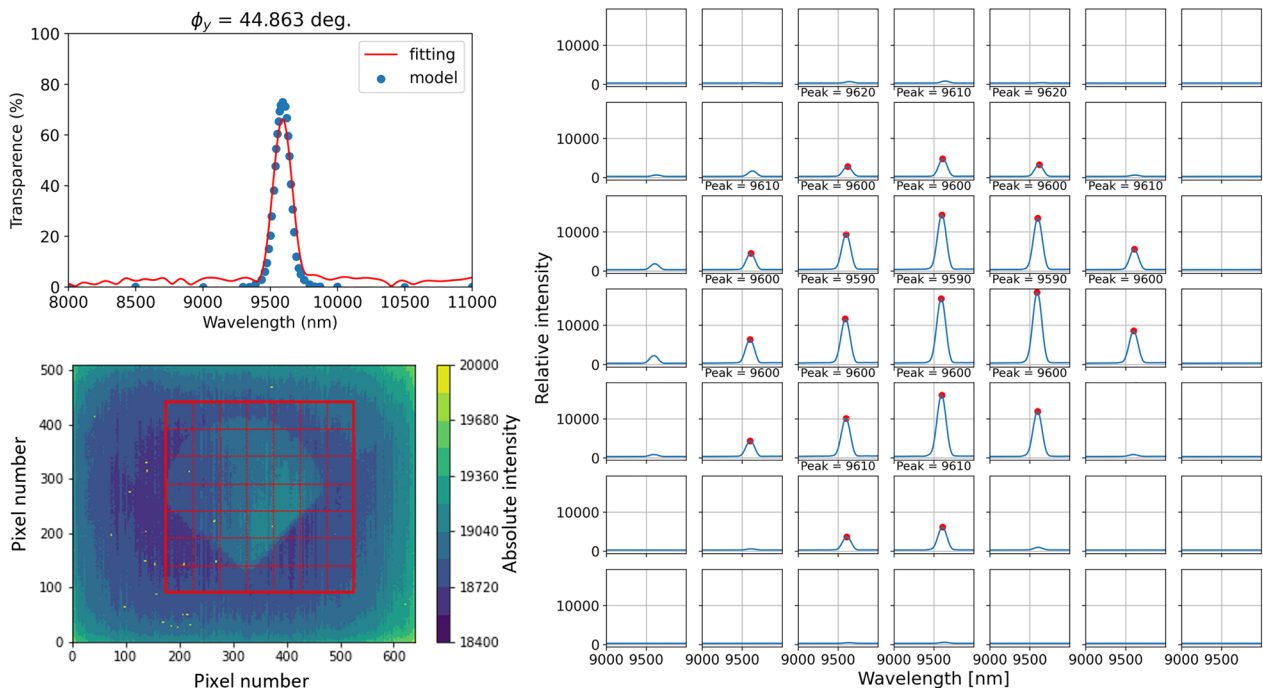


Fig. 6 (Left top) The spectrum of official transmittance data of BPF (model) and that measured by 2D FT-IR and calibrated by view angle correction (fitting). x and y coordinates show the pixel number of the detector (Left bottom) Image of the interferogram of $N=400$, which is near the center burst. The fan shape is the area where the light is transmitted through BPF. (Right) Spectral map averaged in the range of 35×35 pixels shown in red grids shown in the left bottom panel. The red dots show the peak positions of the spectra with peak heights

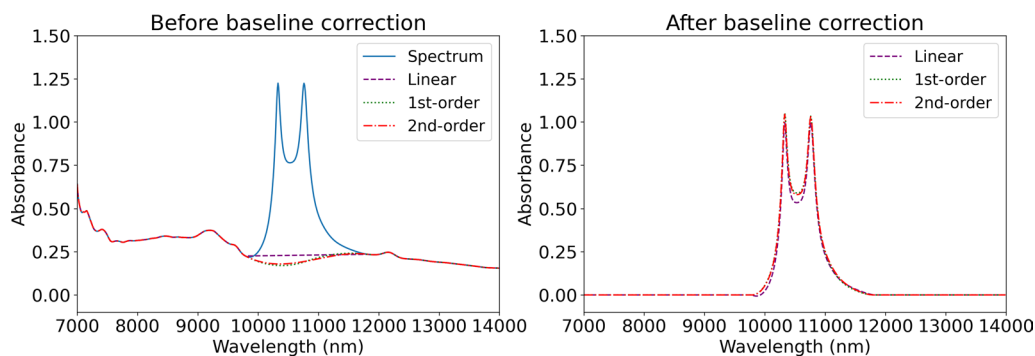


Fig. 7 (Left) Example absorbance spectrum (solid line) with baselines. The baselines using zero-order (linear), first-order, and second-order polynomials are shown by dashed, dotted, and dashed–dotted lines, respectively. (Right) Spectrum after subtraction of the baselines

Table 2 Detected C_2H_4 bands in the experiment

Wavelength (μm)	Band	Vibration mode	Baseline range (μm)	Peak absorbance*
6.9	$C_2H_4 \nu_{12} (B_{3u})$	Out-of-plane	6.00–6.84, 7.07–14.00	0.4
10.4, 10.6	$C_2H_4 \nu_7 (B_{1u})$	In-plane	7.00–9.80, 11.80–14.00	1.0
12.2	$C_2H_4 \nu_{10} (B_{2u})$	In-plane	7.00–11.90, 12.60–14.00	0.03

* 1 The data with baseline correction at the center of the aperture were measured 26 min after the first gas input

and 11.8–14.0 μm . The absorbance of the first-order baseline was larger than that of the linear baseline. It shows the absorbance may be underestimated if the linear baseline is used. In this study, the original spectra were differenced at the second-order baseline. Finally, we detected three C_2H_4 absorption bands of the bending vibration mode as shown in Table 2. We confirmed that spectra below 7.0 μm and above 12.0 μm are obtainable, even with the deteriorated signal-to-noise ratio (S/N). It suggests the possibility of the measurements of other important hydro-carbon frosts such as CH_4 and C_2H_6 by 2D FT-IR in the future.

Results

Spectral maps of the ν_7 band in 11×11 bins are illustrated in Fig. 8, in which the 3 mm ϕ aperture in the sample holder is shown in the black solid circle of top spectral images. The spectrum for each bin is the average of the data in the range of 30×30 pixels, corresponding to $\sim 400 \times 400 \mu m$ on the detector. The untrustworthy spectra of gray bins in the maps are removed since they seem to be outside the edges of the aperture, and therefore almost no light is transmitted. The two-dimensional absorption spectra of C_2H_4 in the out-of-plane bending mode ν_7 vibrational band at about 10 μm were obtained in all measurements.

Initially, a single spectral line at 10.6 μm of ν_7 band was identified in all spectral bins without bottom edges of the aperture when the C_2H_4 partial pressure was ~ 700 Pa.

After 10 min from the first gas input, the spectral shape at any bin did not change and the peak absorbance slightly decreased. The uniformity of the spectra indicates that the IR absorption was mainly caused by gaseous C_2H_4 . At the same time, the absorptions of ν_{10} and ν_{12} bands were not detected. After 26 min, when the C_2H_4 partial pressure was ~ 1000 Pa, the spectral map of the ν_7 band showed a significant change in spectral shape with two absorption peaks except for the top and bottom edges of the aperture. The ununiform spectra suggest that the condensation of the C_2H_4 frost started at this time. On the other hand, the spectral shapes of ν_{10} and ν_{12} bands shown in Fig. 9 are single peaks regardless of the place. One possible speculation for the reason for different spectral shapes between the ν_7 band and ν_{10} and ν_{12} bands is that out-of-plane bending is greatly affected when C_2H_4 aggregates and π – π stacking occurs. After 35 min, the spectral absorbance slightly increased, suggesting the growth of the frost. Hereafter we call the initial data “before condensation” and the data after 26 min from the first gas input “after condensation”.

To understand the detailed properties of the spectral shapes, the spectra before condensation were fitted to the single Gaussian function $f(x)$ shown in Fig. 10:

$$f(x) = a \cdot \exp\left\{-\frac{(x - \mu)^2}{2\sigma^2}\right\} \quad (12)$$

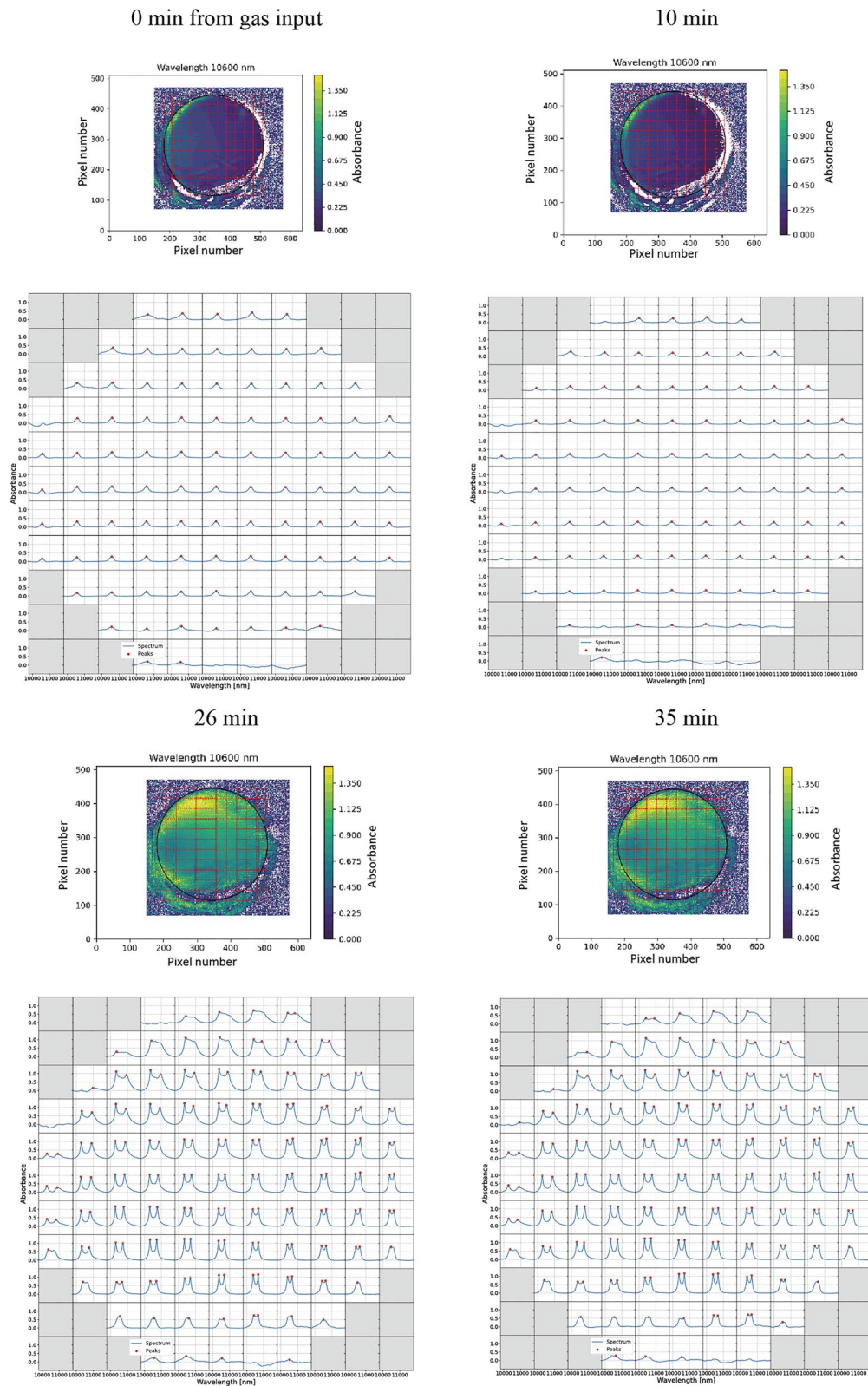


Fig. 8 (Top) Absorbance spectral images at the wavelength of 10.6 μm . x and y coordinates correspond to the pixel number of the detector. The black solid circle shows the expected field of view, which corresponds to the boundary of the aperture of the sample holder. (Bottom) Spectral maps in the same region of the top figures. The red dots show the peak positions of the spectra

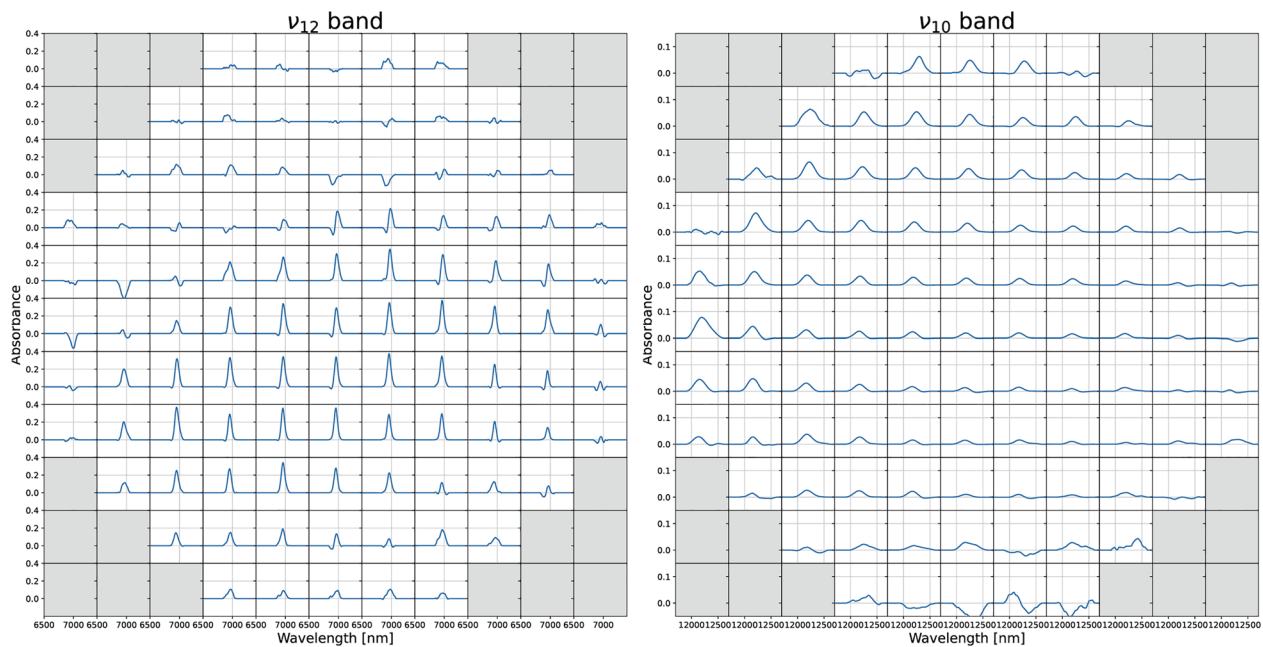


Fig. 9 (Left) Absorbance spectral map of 6.9 μm C_2H_4 ν_{12} band after 26 min from the first gas input. (Right) Same but 12.2 μm C_2H_4 ν_{10} band

where x represents the wavelength of the data point, and fitting parameters a , and μ represents the peak height and peak wavelength, respectively. The full-width at half-maximum (FWHM) is $2\sqrt{2\ln 2}\sigma$. The error of each parameter is equal to the square root of the diagonal component of the variance–covariance matrix. The area filled between x -axis and a single Gaussian function is defined as $\sqrt{2\pi}a\sigma$. Error propagation was considered to estimate the error of area. The correlation between a and σ was not taken into account. The left side of Fig. 11 shows contour maps of peak height, peak wavelength, FWHM, and area of the fitting function. The maps of these errors on the right side of Fig. 11 show fitting accuracy is high except for the left top and bottom edge of the aperture such as the non-detection part of (i_1, j_4) , (i_7, j_{11}) , and (i_8, j_{11}) . The position of the maximum area is (i_5, j_6) , which is thought to be the center where the gas is blown directly. Because both peak height and FWHM are roughly correlated with the area of the Gaussian function, spectral shapes are almost the same regardless of the place of frost on the plate.

The map of spectra after condensation with fitting is shown in Fig. 12. Because most of the spectral shapes are double peaks, fitting to a single Gaussian function is not suitable. Using the double Gaussian function, the accuracy of fitting to the spectrum after condensation is low, especially at the wavelength of the steep gradients around the peaks. Therefore, we fitted the spectrum to the double Lorentzian function $g(x)$:

$$g(x) = g_1(x) + g_2(x) = \frac{a_1\sigma_1}{(x - \mu_1)^2 + \sigma_1^2} + \frac{a_2\sigma_2}{(x - \mu_2)^2 + \sigma_2^2} \quad (13)$$

$g_1(x)$ and $g_2(x)$ are blue and red-shifted components, respectively. x is the wavelength of the data point, σ_1 , σ_2 are the half of FWHM, and μ_1 , μ_2 are wavelength at the peak position ($\mu_1 < \mu_2$). Peak heights can be represented as

$$g_1(\mu_1) = a_1/\sigma_1 \quad (14)$$

$$g_2(\mu_2) = a_2/\sigma_2 \quad (15)$$

where a_1 , a_2 are the fitting parameters ($a_1 > 0$, $a_2 > 0$). In the top of Fig. 12, the spectral peaks are negative in the non-detection part of (i_1, j_4) , (i_4, j_1) , and (i_7, j_{11}) . The coefficient of determination of a fit is less than $R^2 = 0.9$ in the regions of (i_2, j_3) and (i_8, j_{11}) . In the rest of the regions, the coefficient is greater than $R^2 = 0.9$, which shows the fitting accuracy is sufficient. According to the maps of fitting parameters in Fig. 13, the distance between the peaks is large on the left side, and it is small on the right side. The large difference in FWHM of the blue-shifted component does not appear. However, that of the red-shifted component is large on the top side compared to the other place. It is the factor that the spectral shapes on the top side are single peaks with gentle slopes in the long wavelength direction [e.g., (i_4, j_2)] or double peaks with different peak heights [e.g., (i_3, j_4)]. On the other

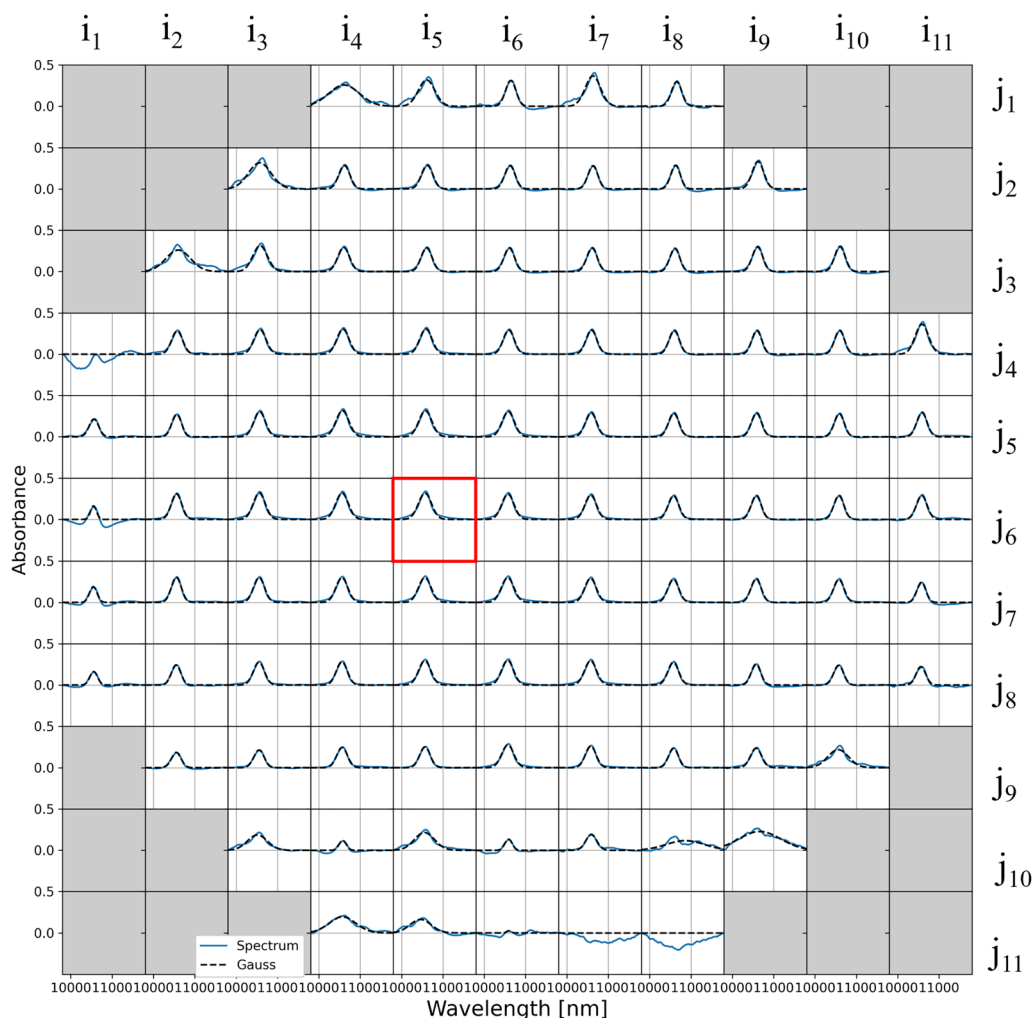


Fig. 10 Absorbance spectral maps of the data measured before condensation. *i* and *j* correspond to the x and y coordinates of the bin. Dashed lines are the results of fitting by a single Gaussian function. The red frame shows the coordinate which is shown in the text

hand, the spectral shape on the middle and bottom sides are double peaks with symmetry height. The single peak structure appears in the bottom edge of the aperture such as (i_3, j_{10}) . We considered the reason of the position sensitive spectra is the different deposition rates between the place that the gas directly collided and the place that the gas spread after collision.

The frost thickness of C_2H_4 can be estimated by Beer–Lambert law, which is that the absorbance peak (I/I_0) is equal to the multiplication of the absorption coefficient and light path:

$$\alpha L = -\log_e \left(\frac{I}{I_0} \right) \tag{16}$$

where α is absorption coefficient, L is light path, which is equal to the frost thickness in case that the angle of incidence is 90° . Hudson et al. (2014) calculated the

absorption coefficients of the ν_{12} band to be 13,180 and $13,620 \text{ cm}^{-1}$ under the Metastable phase. In the top and middle regions of the map, peak absorbances of most spectra are around 1. If their data are used directly, the estimated frost thickness is $\sim 3.3 \mu\text{m}$ in these regions.

Discussion

Comparison to other experimental results

According to Hudson et al. (2014), both Metastable and Crystalline appear to have double peaks and valleys between them. In Crystalline, the distance between the peaks is smaller and the depth of the valley becomes shallower than in Amorphous. Referring to their study, we classified the spectral map in Fig. 12 using a histogram in Fig. 14 as follows:

1. In case either peak absorbance $g_1(\mu_1)$ or $g_2(\mu_2)$ is below 0.1, the double gaussian fitting to the spectrum

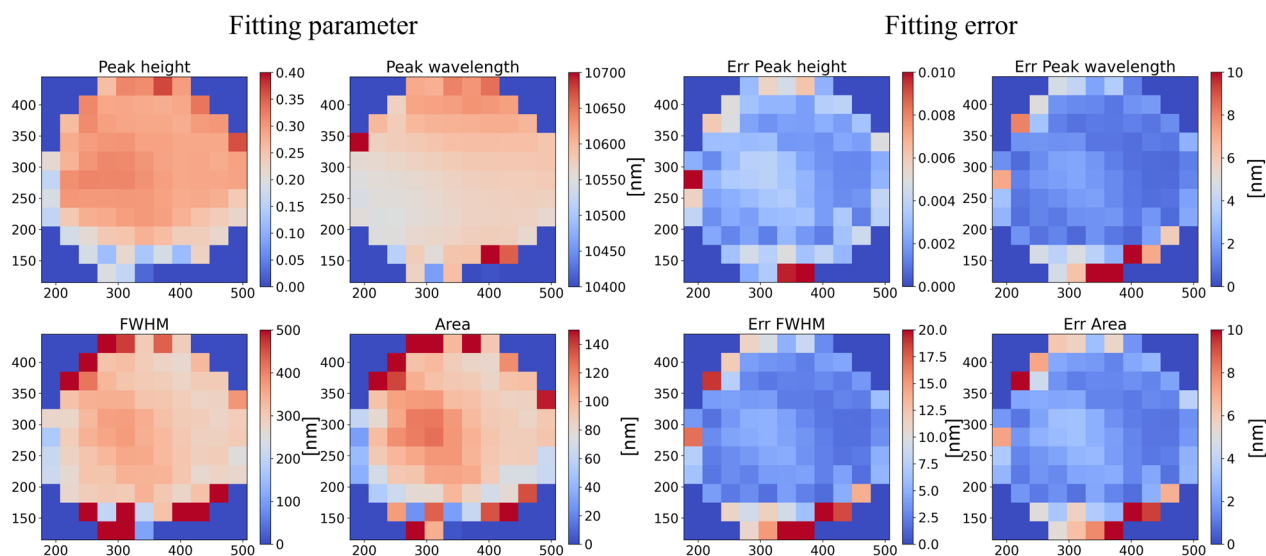


Fig. 11 (Left) Maps of the fitting parameters of Fig. 10. x and y coordinates show the pixel number of the detector (same as Fig. 13 and Fig. 16). Definitions of the parameters are shown in the text. (Right) Maps of Errors of the fitting parameters

is failed (the background of the map is filled in gray). If it is over 0.1, we consider the absorption of solid C_2H_4 is detected with sufficient S/N.

2. In case the FWHM of the red-shifted component σ_2 is over 390, the spectrum is categorized as “type 1” (white)

If conditions 1 and 2 are not satisfied,

3. In case the distance between the peaks $\mu_2 - \mu_1$ is over 335, the spectrum is categorized as “type 2” (green). It includes the estimated center position where the gas is blown directly (see Results).
4. In the case that $\mu_2 - \mu_1$ is under 335, the spectrum is categorized as “type 3” (blue).

Except for (i_1, j_7) and (i_5, j_{11}) , three regions of white, blue, and green colors are separated. The spectra of type 1, type 2, and type 3 are distributed in the top, middle left, and the other side in the spectral map of Fig. 12, respectively. In Fig. 15, we plotted the representative spectrum at points (i_4, j_2) of type 1, at (i_5, j_5) of type 2, and (i_9, j_7) of type 3 in this study. The spectra in Hudson et al. (2014) are also superimposed. It is noted that the wavenumber resolution of their study is 1 cm^{-1} , which is 7 times better than this study. It can be seen from the diagram that the line shapes of the spectra of type 1, type 2, and type 3 are roughly similar to Hudson’s spectra under the phases of amorphous, metastable, and crystalline, respectively.

However, it is clear that the distance between peaks 1 and 2 in this study is greater than that in Hudson’s results, and there is some variation in the shape of the peaks for Amorphous. In Hudson’s study, the out-of-plane bending vibration ν_7 of C_2H_4 at wavelengths of $10 < \lambda < 11 \text{ }\mu\text{m}$ has only a single peak at about $10.53 \text{ }\mu\text{m}$ in the case of amorphous ice. In the state of Metastable ice, the peak becomes double at the wavelength of $10.52 \text{ }\mu\text{m}$ and $10.63 \text{ }\mu\text{m}$, respectively. The difference between the peaks is $0.11 \text{ }\mu\text{m}$. When it becomes crystalline ice, the distance between the two peaks becomes smaller, causing the shape of the double peak to change. The peaks change at $10.54 \text{ }\mu\text{m}$ and $10.60 \text{ }\mu\text{m}$, respectively, with a difference of $0.06 \text{ }\mu\text{m}$. In contrast, in this study, a single peak of the spectrum at point (i_4, j_2) of type 1 appears at the wavelength of $10.40 \text{ }\mu\text{m}$. The difference in absorption peaks at (i_5, j_5) of type 2 and (i_9, j_7) of type 3 are $0.39 \text{ }\mu\text{m}$ and $0.3 \text{ }\mu\text{m}$, respectively. The spectrum with a peak difference under $0.14 \text{ }\mu\text{m}$ is not found. The discrepancy in the peak separations between Hudson et al. (2014) and the present study may result from the difference in deposition temperature and subsequent annealing. The possible reason for an inconsistent distance between the bimodal peaks is a gap at the temperature level. In Hudson’s experiments, Crystalline was obtained by slow deposition of and cooling the C_2H_4 solid from 60 to 20 K; Metastable was obtained by rapid deposition at 20 K; Amorphous was obtained by heating the C_2H_4 solid from 12 to 20 K. On the other hand, the temperature for the experiments in this study was constant at around 83 K. It suggests that

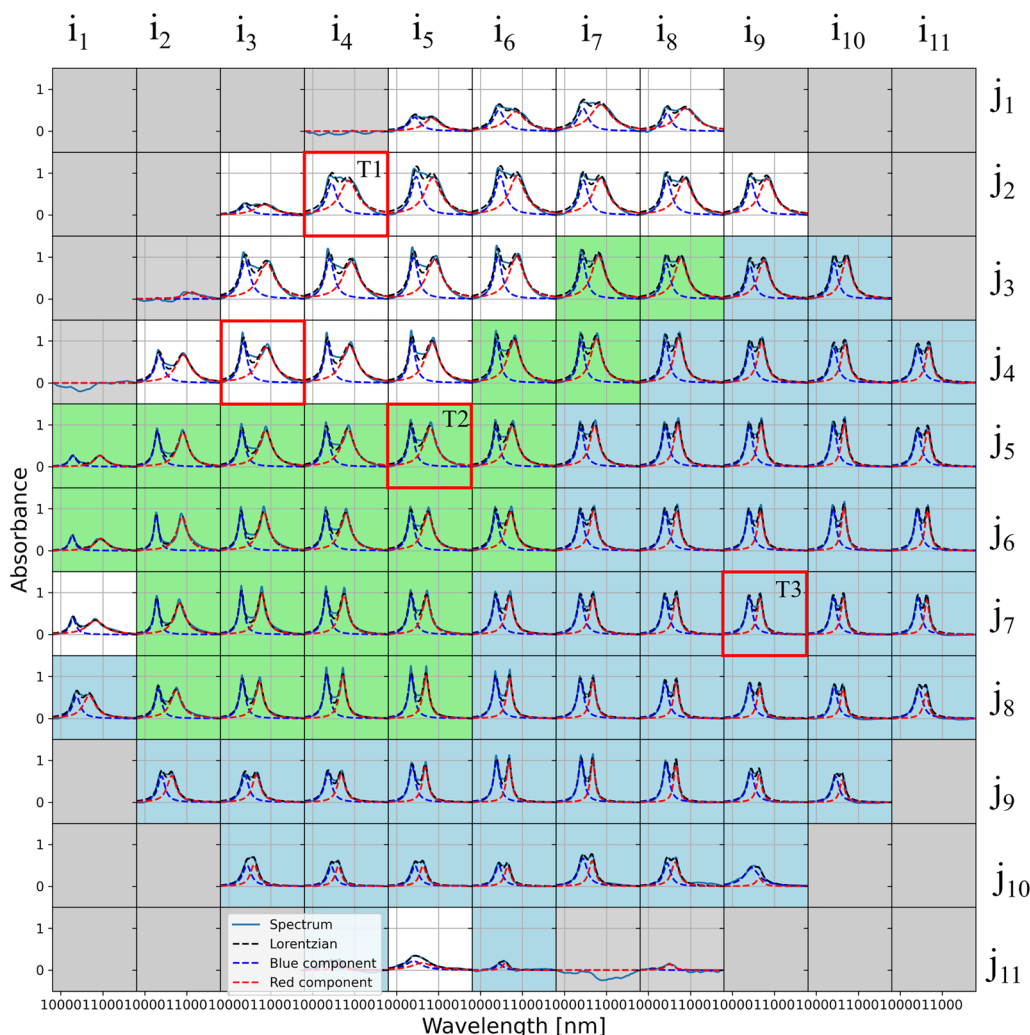


Fig. 12 Absorbance spectral maps after condensation. Dashed lines are the results of fitting by the double Lorentzian function. T1, T2, and T3 show the representative spectra of type 1, type 2, and type 3 shown in the text, respectively

the C₂H₄ solid may have a different crystal structure in 20 K and 83 K environments.

Classical oscillator model of C₂H₄

The ν₇ vibration spectrum of the solid C₂H₄ measured in this study can be described by the classical mechanical spring model. In the Lorentz oscillator model, electrons are bound to the atomic nucleus analogously to springs of different strengths. In spectroscopy, the Lorentz model describes the shape of a spectral line that is broadened by resonance or other mechanisms. The electrical dipoles here are spring-bound positive and negative charges and are regarded as harmonic oscillators whose vibration resistance is proportional to the speed of movement. In real molecules, the mass of the nucleus is much greater than that of the electron, so an approximation can be made by considering the electron

only as changing its position due to fluctuations in the electric field. The complex dielectric function is

$$\epsilon_r = \epsilon_{r,\infty} + \frac{N_{osc}q^2}{m \epsilon_0} \frac{1}{(\omega_0^2 - \omega)^2 + \gamma^2\omega^2} = \epsilon_1 + \epsilon_2 \tag{17}$$

ε_{r,∞} are short wavelength and long wavelength infinity of ε_r, N_{OSC} is number of oscillators per unit volume, q is effective electric charge, m is effective mass, ε₀ is vacuum dielectric constant, γ is damping factor, ω and ω₀ are the angular frequency and natural angular frequency, respectively. The real component ε₁ of ε_r is known as the resonant component and the imaginary component ε₂ corresponding to the decay of the electric field is known as the absorption component:

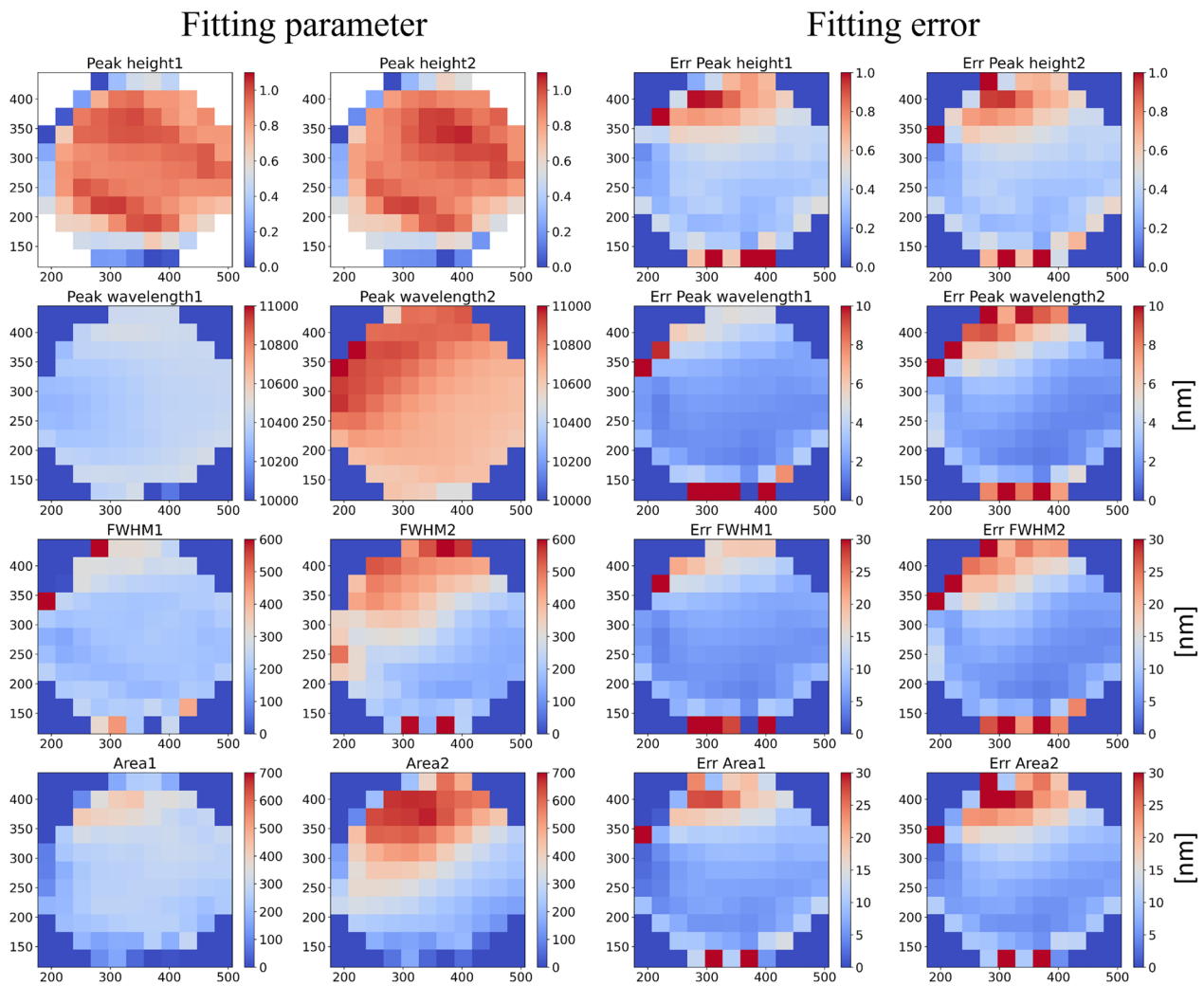


Fig. 13 (Left) Maps of the fitting parameters of Fig. 12. Definitions of the parameters are shown in the text. (Right) Maps of errors of the fitting parameters

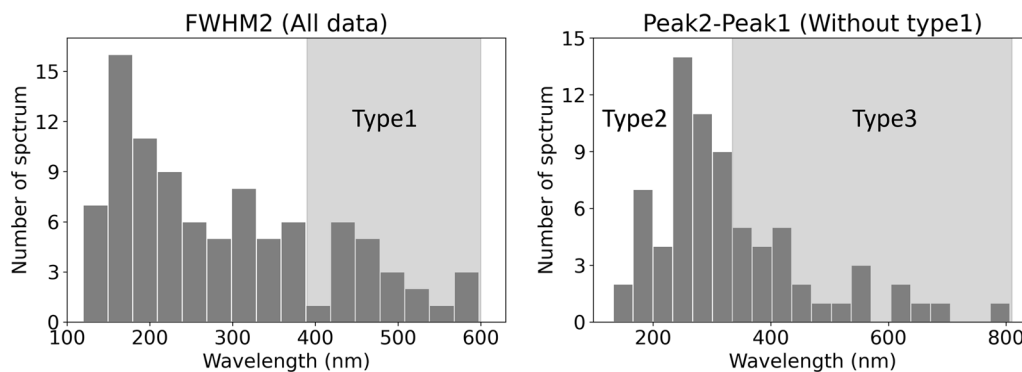


Fig. 14 (Left) Histogram of FWHM of the red-shifted component with all data (Right) Histogram of the distance of the peaks with data excluding type 1

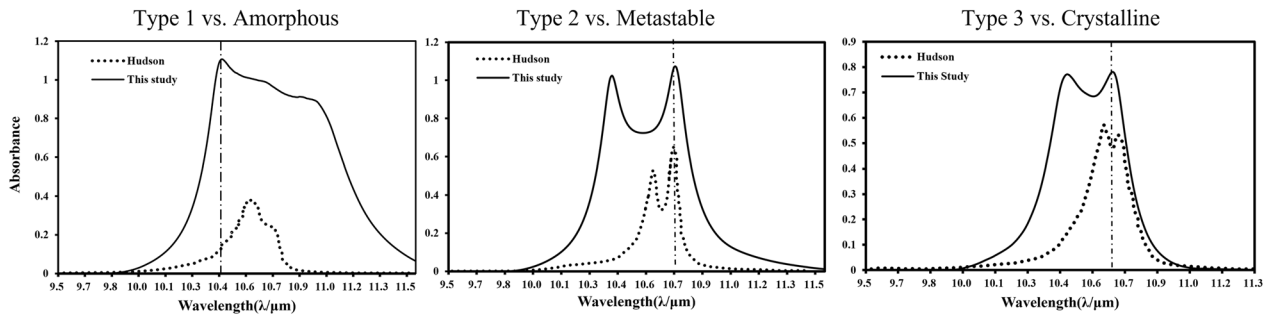


Fig. 15 Representative spectra of a single peak, type 2 and type 3 in this study (solid lines), and spectra under the phases of Amorphous, Metastable, and Crystalline in Hudson et al. (2014) (dashed lines)

$$\varepsilon_1 = \varepsilon_{r,\infty} + \frac{N_{\text{OSC}} q^2}{m \varepsilon_0} \frac{\omega_0^2 - \omega^2}{(\omega_0^2 - \omega)^2 + \gamma^2 \omega^2} \quad (18)$$

$$\varepsilon_2 = \frac{N_{\text{OSC}} q^2}{m \varepsilon_0} \frac{\gamma \omega}{(\omega_0^2 - \omega)^2 + \gamma^2 \omega^2} \quad (19)$$

Only the absorption component of the electric field can be measured in this study. This equation can be approximated in terms of wavenumber $\tilde{\nu} = \omega/2\pi c_0$

$$\varepsilon_2 \sim \frac{1}{(2\pi c)^2} \frac{N_{\text{OSC}} q^2}{m \varepsilon_0} \frac{\gamma'}{(\tilde{\nu}_0 - \tilde{\nu})^2 + (\gamma'/2)^2} \quad (20)$$

$$\gamma' = \frac{\gamma}{2\pi c} \quad (21)$$

Finally, the damping factors in Fig. 16 are derived by the fitting of the double Lorentzian fitting to the spectral data with the horizontal axis converted to wavenumber. In this experiment, the averaged factors of blue- and red-shifted components where the fitting is succeeded are estimated to be 3.7×10^{12} , and 4.6×10^{12} s, respectively.

They are larger than the coefficients derived by the double Lorentz fitting of Hudson's spectra, which are estimated to be 3.1×10^{12} and 1.5×10^{12} s under the metastable phase and to be 2.2×10^{12} and 9.2×10^{11} s under the phase of crystalline, respectively. A further experiment that realizes various changes in deposition conditions and theoretical simulation (Ito et al. 2023) will be needed to verify that the C_2H_4 solid has a different crystal structure and damping timescale of oscillation in 20 K and 83 K environments.

Summary

In this study, the authors used a self-developed cryogenic infrared optical device for performing laboratory simulations of the formation and in-situ infrared spectroscopic measurements of low-temperature C_2H_4 solids. In this experiment, two-dimensional IR spectra of the out-of-plane bending vibration ν_7 and in-plane bending vibration ν_{10} and ν_{12} bands of C_2H_4 solid were obtained by measurement at a low temperature of ~ 83 K. Various spectral shapes are found such as the single peak in the edge region, the double-peaked region with deeper valleys, and the double-peaked region with shallower

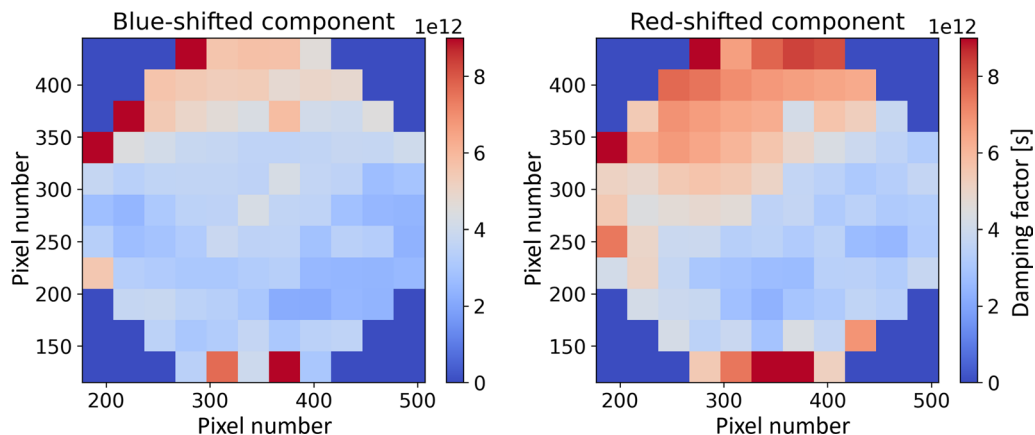


Fig. 16 Distribution of the damping coefficients of the blue-shifted and red-shifted components estimated in this study

valleys. The double Lorentzian function was used to perform a least-squares fit to the obtained C₂H₄ IR spectra. Then, we tried to classify their spectral shapes referencing those of Hudson et al. (2014) under the phase of amorphous, metastable, and crystalline. However, the distance between the peaks observed in this study is much larger than the previous study possibly because of the difference in the sample plate temperature.

Abbreviations

IR	Infrared
OFHC	Oxygen-Free High-Conductivity Copper
FFT	Fast Fourier Transform
2D FT-IR	Imaging Fourier transform mid-infrared spectrometer
BPF	Bandpass Filter
FWHM	Full-width at half-maximum
S/N	Single-to-Noise

Acknowledgements

The authors thank the Nagoya University Instrument Development Center for creating the vacuum chamber and repairing the dewar bottle. The authors consulted with NISSIN KIKAI Co. and Dr. Qi Wei about the mechanism of 2D FT-IR and the data analysis method of FFT.

Author contributions

RK summarized the data and wrote the manuscript with contributions from SN, BZ, and YH. FI contributed to writing the manuscript and supported the experiment. YL prepared the figures in this paper. YK set up the instruments and supported the experiment.

Funding

This work was supported by JSPS KAKENHI Grant Numbers JP21J00734, JP22K14084, JP20KK0074, JP19H01950, JP21K18640. This work was carried out by the joint research program of the Institute for Space–Earth Environmental Research, Nagoya University.

Availability of data and materials

Raw data were generated at the Department of Earth and Planetary Sciences, Graduate School of Environmental Studies, Nagoya University. Derived data supporting the findings of this study are available from the corresponding author RK and co-author YH on request. FFT codes we developed were uploaded to the platform of GitHub (https://github.com/RyoichiKoga/Py2DF_TIR). The transmittance data of BPF NB-9585–135 can be imported from the IR system site (<https://www.irsytem.com/stock/filter/bpf/>).

Declarations

Ethics approval and consent to participate.

Not applicable.

Consent for publication

Not applicable.

Competing interests

The authors declare that they have no competing interests.

Author details

¹ Graduate School of Environmental Studies, Nagoya University, Nagoya, Aichi 464-8601, Japan. ² National Institute of Advanced Industrial Science and Technology (AIST), Onogawa 16-1, Tsukuba, Ibaraki 305-8569, Japan. ³ Planetary Plasma and Atmospheric Research Center, Graduate School of Science, Tohoku University, Sendai, Miyagi 980-8578, Japan.

Received: 25 July 2023 Accepted: 28 January 2024

Published online: 18 February 2024

References

- Cernicharo J, Heras AM, Tielens AGGM, Pardo JR, Herpin F, Guélin M, Waters LBFM (2001) Infrared space observatory discovery of C₄H₂, C₆H₂, and benzene in CRL 618. *Astrophys J* 546(2):L123–L126. <https://doi.org/10.1086/318871>
- Fray N, Schmitt B (2009) Sublimation of ices of astrophysical interest: a bibliographic review. *Planet Space Sci* 57(14–15):2053–2080. <https://doi.org/10.1016/j.pss.2009.09.011>
- Gladstone GR, Stern SA, Ennico K, Olkin CB, Weaver HA, Young LA, Summers ME, Strobel DF, Hinson DP, Kammer JA, Parker AH, Steffl AJ, Linscott IR, Parker JW, Cheng AF, Slater DC, Versteeg MH, Greathouse TK, Retherford KD, Zirmstein E (2016) The atmosphere of Pluto as observed by New Horizons. *Science* 351(6279):8866–8871. <https://doi.org/10.1126/science.aad8866>
- Grundy WM, Bertrand T, Binzel RP, Buie MW, Buratti BJ, Cheng AF, Cook JC, Cruikshank DP, Devins SL, Dalle Ore CM, Earle AM, Ennico K, Forget F, Gao P, Gladstone GR, Howett CJA, Jennings DE, Kammer JA, Lauer TR, Zhang X (2018) Pluto's haze as a surface material. *Icarus* 314:232–245. <https://doi.org/10.1016/j.icarus.2018.05.019>
- Hörst SM (2017) Titan's atmosphere and climate. *J Geophys Res Planets* 122(3):432–482. <https://doi.org/10.1002/2016JE005240>
- Hudson RL, Moore MH, Raines LL (2009) Ethane ices in the outer solar system: spectroscopy and chemistry. *Icarus* 203(2):677–680. <https://doi.org/10.1016/j.icarus.2009.06.026>
- Hudson RL, Gerakines PA, Moore MH (2014) Infrared spectra and optical constants of astronomical ices: II. Ethane Ethylene *Icarus* 243:148–157. <https://doi.org/10.1016/j.icarus.2014.09.001>
- Inoue Y, Ishimaru I, Yasokawa T, Ishizaki K, Yoshida M, Kondo M, Kuriyama S, Masaki T, Nakai S, Takegawa K, Tanaka N (2006) Variable phase-contrast fluorescence spectrometry for fluorescently stained cells. *Appl Phys Lett* 89(12):2003–2006. <https://doi.org/10.1063/1.2356312>
- Ishimaru I. (2012) JP patent. 2012: 181060 <https://www.jp-platpat.inpit.go.jp>.
- Ito F, Koga R, Negishi S, Hirahara Y (2023) UV irradiation and infrared observation of sulfur dioxide clusters and solids at cryogenic temperature. *Chem Phys Lett* 829:40742. <https://doi.org/10.1016/j.cplett.2023.140742>
- Jacox ME (1962) Solid-state vibrational spectra of ethylene and ethylene-d 4. *J Chem Phys* 36(1):140–143. <https://doi.org/10.1063/1.1732284>
- Lorenz RD, Lemmon MT, Smith PH, Lockwood GW (1999) Seasonal Change on titan observed with the hubble space telescope WFPC-2. *Icarus* 142(2):391–401. <https://doi.org/10.1006/icar.1999.6225>
- Magee BA, Waite JH, Mandt KE, Westlake J, Bell J, Gell DA (2009) INMS-derived composition of Titan's upper atmosphere: analysis methods and model comparison. *Planet Space Sci* 57(14–15):1895–1916. <https://doi.org/10.1016/j.pss.2009.06.016>
- Mitri G, Showman AP, Lunine JI, Lorenz RD (2007) Hydrocarbon lakes on Titan. *Icarus* 186(2):385–394. <https://doi.org/10.1016/j.icarus.2006.09.004>
- Molpeceres G, Satorre MA, Ortigoso J, Zanchet A, Luna R, Millán C, Escibano R, Tanarro I, Herrero VJ, Maté B (2017) Physical and spectroscopic properties of pure C₂H₄ and CH₄:C₂H₄ ices. *Mon Not R Astron Soc* 466(2):1894–1902. <https://doi.org/10.1093/mnras/stw3166>
- Nes GJH, Vos A (1979) Single-crystal structures and electron density distributions of ethane, ethylene and acetylene. III. Single-crystal X-ray structure determination of ethylene at 85 K. *Acta Cryst* 35(11):2593–2601. <https://doi.org/10.1107/S0567740879009961>
- Niemann HB, Atreya SK, Bauer SJ, Carignan GR, Demick JE, Frost RL, Gautier D, Haberman JA, Harpold DN, Hunten DM, Israel G, Lunine JI, Kasprzak WT, Owen TC, Paulkovich M, Raulin F, Raaen E, Way SH (2005) The abundances of constituents of Titan's atmosphere from the GCMS instrument on the Huygens probe. *Nature* 438(7069):779–784. <https://doi.org/10.1038/nature04122>
- Nogo K, Qi W, Mori K, Ogawa S, Inohara D, Hosono S, Kawashima N, Nishiyama A, Wada K, Ishimaru I (2016) Ultrasonic separation of a suspension for in situ spectroscopic imaging. *Opt Rev* 23:360–363. <https://doi.org/10.1007/s10043-016-0186-x>
- Nogo K, Ikejima K, Qi W, Mori K, Kawashima N, Kitazawa T, Adachi S, Wada K, Nishiyama A, Ishimaru I (2021) Identification of black microplastics using longwavelength infrared hyperspectral imaging with imaging-type two-dimensional Fourier spectroscopy. *Anal Methods* 13:647–659. <https://doi.org/10.1039/D0AY01738H>

- Polavarapu PL (1985) Fourier transform infrared vibrational circular dichroism. In: Ferraro JR, Basile LJ (eds) *Fourier transform infrared spectroscopy*. Academic Press, Cambridge
- Qi W, Suzuki Y, Sato S, Fujiwara M, Kawashima N, Suzuki S, Abeygunawardhana P, Wada K, Nishiyama A, Ishimaru I (2015) Enhanced interference-pattern visibility using multislit optical superposition method for imaging-type two-dimensional Fourier spectroscopy. *Appl Opt* 54(20):6254. <https://doi.org/10.1364/ao.54.006254>
- Qi, W. (2016), Study on Fundamental Technologies of the Wide field Infrared Fourier Spectroscopic Imaging, Doctoral thesis, Kagawa University.
- Roe HG, de Pater I, McKay CP (2004) Seasonal variation of Titan's stratospheric ethylene (C₂H₄) observed. *Icarus* 169(2):440–461. <https://doi.org/10.1016/j.icarus.2004.01.002>
- Rytter E, Gruen DM (1979) Infrared spectra of matrix isolated and solid ethylene. Formation of ethylene dimers. *Spectrochim Acta Part A* 35(3):199–207. [https://doi.org/10.1016/0584-8539\(79\)80137-3](https://doi.org/10.1016/0584-8539(79)80137-3)
- Smith BA, Soderblom L, Batson R, Bridges P, Inge J, Masursky H, Shoemaker E, Beebe R, Boyce J, Briggs G, Bunker A, Collins SA, Hansen CJ, Johnson TV, Mitchell JL, Terrile RJ, Cook AF, Cuzzi J, Pollack JB, Suomi VE (1982) A new look at the Saturn system: the Voyager 2 images. *Science* 215(4532):504–537. <https://doi.org/10.1126/science.215.4532.504>
- Teolis BD, Wyrick DY, Bouquet A, Magee BA, Waite JH (2017) Plume and surface feature structure and compositional effects on Europa's global exosphere: Preliminary Europa mission predictions. *Icarus* 284:18–29. <https://doi.org/10.1016/j.icarus.2016.10.027>

Publisher's Note

Springer Nature remains neutral with regard to jurisdictional claims in published maps and institutional affiliations.